Gas-mediated trace element incorporation into rhyolite-hosted topaz: A synchrotron microbeam XAS study

D.R. SCHAUB¹, PAUL NORTHRUP¹, HANNA NEKVASIL^{1,*}, TRISTAN CATALANO¹, AND RYAN TAPPERO²

¹Department of Geosciences, Stony Brook University, Stony Brook, New York 11794-2100, U.S.A. ²National Synchrotron Light Source II, Brookhaven National Laboratory, Upton, New York 11973, U.S.A.

ABSTRACT

Magmatic gas exsolving during late-stage cooling of shallow magmas has been considered an important facilitator of low-pressure alteration and metal transport. However, the chemical properties of such gas, particularly its metal transport mechanisms and capacity, remain elusive. Trace elements in minerals produced by gas-mediated surface reaction or precipitation from gas capture details of gas composition and reaction pathways. However, interpretation of mineral trace element contents is dependent on understanding crystallographic controls on gas/mineral partitioning. This work investigates the structural accommodation of As, Mn, Ga, Ge, Fe, and Ti in vapor-deposited topaz of vesicular topaz rhyolite from the Thomas Range. Utah, through single-crystal synchrotron microbeam X-ray techniques on picogram quantities of those trace elements. X-ray absorption near edge structure (XANES) data indicates that these elements are incorporated into topaz as As5+, Fe3+, Mn3+, Ti4+, Ga3+, and Ge⁴⁺. Extended X-ray absorption fine structure (EXAFS) analysis for these trace elements, compared to EXAFS of structural Al and Si, reveals that As5+ and Ge4+ are incorporated directly into the tetrahedral site of the topaz structure, with the octahedral site accommodating Mn³⁺, Fe³⁺, Ga³⁺, and Ti⁴⁺. For As⁵⁺ and Fe³⁺, the structural impact of substitution extends to at least second neighbors (other elements were only resolvable to first neighbors). Further interpretation of the EXAFS results suggests that the substitution of Ti⁴⁺ results in increased distortion of the octahedral site, while the other trace elements induce more uniform expansion correlating in magnitude to their ionic radius. Comparison of quantified X-ray fluorescence (XRF) data for two topaz crystals from this rhyolite reveals variable trace element concentrations for As5+, Fe3+, Ga3+, and Ti4+, reflective of a source gas undersaturated in these trace elements changing in concentration over the period of topaz deposition. The identical Ge⁴⁺ content of the two topaz crystals suggests that Ge4+ in the gas was buffered by the growth of another Ge⁴⁺-bearing phase, such as quartz. The very low Mn³⁺ content in the topaz crystals does not reflect the abundance of Mn³⁺ in the gas (saturation of Mn is evidenced by coexisting bixbyite). Instead, it suggests a strong Jahn-Teller inhibitory effect to the substitution of Mn3+ for Al3+ in the distorted octahedral site of topaz. It is proposed that exsolution of an HF-enriched gas from cooling rhyolitic magma led to local scouring of Al, Si, and trace metals from the magma. Once topaz crystals nucleated, self-catalyzed reactions that recycle HF led to continued growth of topaz.

Keywords: Crystal structure, EXAFS, igneous rocks, magmatic gas, rhyolite, silicates, single-crystal EXAFS, topaz, trace elements, vapor phase, X-ray absorption spectroscopy; Experimental Halogens in Honor of Jim Webster

INTRODUCTION

3 4

5 6

7 8

9

10

11 12

13

14

15

16

17

18

19

20

21

22

23

24

25

26

27

28

29

30

31

32

33

34

35

36

37

38

39

40

41

46

47

48

49

50

51

52

53

54

55

56

57

58

59

Topaz, Al₂SiO₄(F,OH)₂, is associated with shallow intrusive domes and lava flows of F-rich rhyolite, specifically, the "topaz rhyolites" of the extensional regions of western North America (e.g., Burt et al. 1982). It is also found in similar rocks cooled at deeper levels, such as rare-earth element enriched pegmatites (e.g., Goad and Černy 1981; Groat et al. 2014) and the plutonic ongonites of eastern Russia and Mongolia (e.g., Kovalenko and Kovalenko 1976). These rocks share the characteristics of high Si, Fe/Mg, and alkali contents; low Ti, Mg, Ca, and P contents;

Nb, Y, U, Th, Ta, and HREE; and depletion of Eu, Sr, and Co (e.g., Christiansen et al. 1984). Recognition of spatial and genetic links between topaz rhyolite vent complexes and volcanogenic deposits of Be, Li, U, and F (e.g., Lindsey 1977; Bikun 1980; Burt and Sheridan 1981), subvolcanic breccia, porphyry, and greisen deposits of Mo, W, and Sn (e.g., Burt et al. 1982), and F- and Mn-rich base and precious metal veins in volcanic rocks (Bove et al. 2007) (or F-rich skarn replacements in carbonate rocks) makes these rhyolites of particular importance.

mildly peraluminous character; substantial enrichment of Rb, Cs,

Topaz of nearly F-end-member composition is found in isolated gas cavities and gas vent channels within topaz rhyolites (e.g., Burt et al. 1982). Textural relationships suggest that vapor played an integral role in topaz formation as well as in the forma-

^{*} E-mail: hanna.nekvasil@stonybrook.edu. Orcid 0000-0001-7315-4551

[†] Special collection papers can be found online at http://www.minsocam.org/MSA/AmMin/special-collections.html.

3

4

5

6

7

8

Q

10

11

12 13

14

15

16

17

18

19

20

21

22

23

24

25

26

27

28

29

30

31

32

33

34

35

36

37

38

39

40

41

42

43

44

45

46

47

48

49

50

51

52

53

54

55

56

57

58

tion of the associated quartz, bixbyite, hematite, pseudobrookite, spessartine-almandine garnet, Mn-rich beryl, and cassiterite (e.g., Holfert 1978; Christiansen et al. 1980). The unusual nature of this mineral assemblage, its prevalence in topaz rhyolite, and the chemistry of the rhyolite itself, all suggest that the vapor was sourced from the rhyolite at shallow depths (e.g., Lipman et al. 1969). The minerals in the cavities appear to have been precipitated at high temperature and low pressure (e.g., Roedder and Stalder 1988) and therefore, may provide insights into F-rich magmatic gas before it has undergone various scrubbing reactions and lost much of its dissolved metal load.

Topaz associated with topaz rhyolite is known to contain trace elements (e.g., Northrup and Reeder 1994; Schott et al. 2003; Wasim et al. 2011; Breiter et al. 2013a; Agangi et al. 2014) that may provide insights into the chemistry of the magmatic gas involved in topaz production. Northrup and Reeder (1994), in their study of the incorporation of trace elements onto growth surfaces of topaz crystals from Mexico, detected Ti, Fe, Ga, Ge, As, and Nb by synchrotron microbeam X-ray fluorescence and noted that these are present in concentrations below ~500 ppm. In topaz from an ongonite from Transbaikalia, Russia, Agangi et al. (2014) detected Fe, Na, P, Li, B, Be, Nb, Ta, W, Ga, Ba, and REEs among other trace elements. Both sets of workers concluded that these trace elements were not in inclusions or defects, but rather incorporated into the topaz lattice. Northrup and Reeder (1994) based this conclusion on the uniformity of the cathodoluminescence maps and XRF concentrations of most trace element within subsectors in the crystal and their strict adherence to crystallographic controls. Agangi et al. (2014) based this on smooth time-resolved LAICP-MS signals. However, none of these workers were able to document the incorporation sites of the trace elements in the topaz structure.

The topaz F-end-member, Al₂SiO₄F₂, is orthorhombic, with space group Pbnm. Its structure (Alston and West 1928; Pauling 1928; Ribbe and Gibbs 1971) consists of zigzag chains of edgesharing AlO₄F₂ octahedra along the c axis with cross-linking SiO₄ tetrahedra (Fig. 1). Adjacent chains of octahedra are rotated 90° relative to each other. Each aluminum octahedron shares two non-opposing O-O edges with adjoining octahedra; the four corners (oxygen ions) defining these edges are also shared with tetrahedra. Fluorine atoms are on adjacent apices of each octahedron; each F is bonded to 2 Al sites to link adjacent chains (Ribbe and Gibbs 1971). The octahedral site is highly distorted (see Fig. 8 in Northrup and Reeder 1994), with Al-F distances ranging from 1.791 to 1.800 Å and Al-O distances ranging from 1.888 to 1.899 Å. Each SiO₄ tetrahedron bridges across the bend of an octahedral chain along c and also cross-links to two adjacent chains. These tetrahedra are somewhat distorted, with Si-O distances ranging from 1.638 to 1.647 Å. Each O in this structure is coordinated to one Si and two Al sites. The SiO₄ groups only share corners with octahedra.

In the topaz F-end-member, there is one Al site; however, in partially hydroxylated topaz, there are three unique Al environments whose abundances depend on the relative concentrations of OH and F ([AlO₄(OH)₂]⁷⁻, [AlO₄(F)₂]⁷⁻, and [AlO₄OH,F]⁷⁻) (e.g., O'Bannon and Williams 2019). Unlike topaz from metasediments associated with subduction, which are commonly hydroxylated (e.g., O'Bannon and Williams

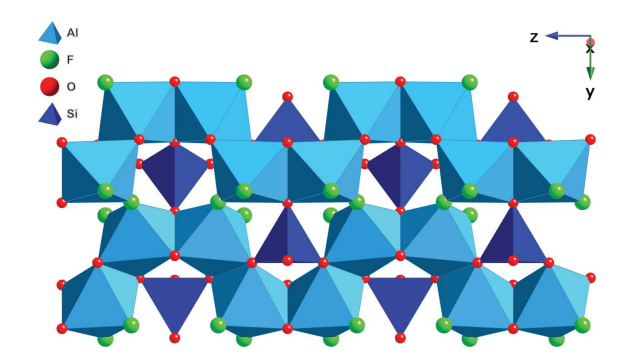


FIGURE 1. Partial view of the topaz crystal structure. Structure parameters from Wyckoff (1969). (Rendering by Crystalmaker). (Color online.)

2019), topaz associated with topaz rhyolites can be assumed to be compositionally close to the F-end-member. This assumption is supported by early measurements of the refractive index of vapor-deposited topaz from the Thomas Range. Penfield and Minor (1894) analyzed F and H₂O in topaz from the Thomas range and found that the amount of water was minor and the F content was very close to that computed for stoichiometric F-end-member. These workers also observed that the physical and optical properties of topaz vary with the fluorine and water content. Later work by Staatz and Carr (1964) noted that all of the topaz they analyzed from the Thomas Range had similar refractive indices, significantly different from those of topaz associated with more water-rich magmas. Such F-rich topaz is also found in ongonites (Agangi et al. 2014). The increase in F/OH ratio of topaz with formation temperature (Thomas 1982) is consistent with topaz forming early during degassing of topaz rhyolite magma.

Northrup and Reeder (1994) and Agangi et al. (2014) speculated that because the topaz structure is based on a dense packing of anions and has little room for interstitial substitution, trace elements probably substitute for Si or Al. On the basis of size considerations, Northrup and Reeder (1994) predicted that Fe³⁺, Ga³⁺, and Mn³⁺ would replace Al³⁺ in the topaz structure, while Ge⁴⁺ would substitute for Si⁴⁺. Since Ti⁴⁺ is too large for the Si tetrahedron they suggested that it substitutes for Al3+ with charge compensation occurring through substitution of O²⁻ for F⁻. Similarly, they predicted that Nb⁵⁺ would replace Al³⁺ with a coupled substitution of 2O2- for 2F-. The complexities of As substitution are compounded by its unknown valence state in topaz. Northrup et al. (1995) reported preliminary As EXAFS results on powdered topaz from a Mexican topaz rhyolite and concluded that As was incorporated into topaz as tetrahedrally coordinated As5+, with an As-O distance of 1.70 (0.02) Å. However, as this was a bulk measurement, they were unable to definitively identify topaz as the host of this As. Based on simple charge balance considerations, Agangi et al. (2014) suggested that trace element incorporation was primarily valence-based, for example, replacement of Si by other cations in the 4+ oxidation state (Ti, V), and replacement of Al3+ by 3+ cations (Ga, Fe, Mn). Uptake of Nb, Ta, and W, which usually occur in the 5+ oxidation state, would require coupled substitution.

To clarify the structural accommodation of As, Mn, Ga, Ge,

10

19

23

24

25

26

27

29

35

39

42

43 44

58

59

Fe, and Ti in F-rich topaz, we obtained detailed information on their crystallographic environment through synchrotron-based X-ray absorption fine structure (XAFS) investigation of singlecrystal topaz at microbeam resolution. Data collection spanned the X-ray absorption near edge structure (XANES) and extended X-ray absorption fine structure (EXAFS) regions. XAFS probes the details of how X-rays are absorbed by an atom at energies near and above the core-level binding energies of that atom. The XANES region is sensitive to oxidation state and coordination chemistry of the absorbing atom; the EXAFS region provides details about an element's local structure (within ~10 Å) in crystalline or non-crystalline materials [e.g., the distances, coordination number, and species of the neighbors of the absorbing atom (Newville 2008)]. For this investigation, we used the hard X-ray microprobe, XFM (which accesses elements from Ca to Zr using their K absorption edges and heavier elements using their L edges) and the tender-energy microprobe TES (Northrup 2019) (which provides unique access to lighter elements Mg through Ca) at NSLS-II (details below).

ANALYTICAL PROCEDURE

Sample characteristics and preparation

The topaz crystal studied here by XAS (Topaz-64) is from Topaz Mountain of the Thomas Range, Utah. The sample is geologically young [6-7 Ma based on the age of the rhyolite (Lindsey 1982)]. It is $4 \times 6 \times 24$ mm in length (along the a, b, and c axes, respectively), and is dominated by (110), with lesser forms (112), (002), (020), (111), (112), and (101) (Fig. 2). A smaller topaz crystal $(2 \times 4 \times 14)$ mm) is attached; this crystal supports a partially embedded 1 mm bixbyite (Mn₂O₃) cube. The lower part of the doubly terminated main crystal encases concentric layers of small quartz crystals and fine-grained rhyolitic matrix. The crystal is transparent with large areas free from visible inclusions. It has pristine surfaces including sharply defined polygonized growth hillocks, indicating the absence of fluid interaction subsequent to crystal formation. Its light sherry color indicates that the crystal was not subjected to heat or exposed to sunlight as either process would render it colorless (e.g., Rossman 2011). The pristine nature of this crystal suggests that it preserves its original trace element budget.

The area chosen for analysis lies on a large $(3 \times 9 \text{ mm})$ polygonized growth hillock on one of the (110) faces [similar to the hillocks studied by Northrup and Reeder (1994, 1995)]. This surface has growth steps aligned along [001] and [110]. For analysis, the sample was mounted intact onto a standard 2" × 2" frame such that the (110) surface faced the beam at 45° and was in the x-y plane of the sample stage, and the c axis was vertical. Initial X-ray fluorescence survey maps (e.g., Online Materials1 Fig. S1) were used to identify an area of uniform composition, free from oxide inclusions that may be rich in the trace elements of interest. The volume of topaz accessed for each element was defined by a beam size of ~10 μm with an effective sampling depth of 10-150 µm depending on incident beam and fluorescence photon energies.

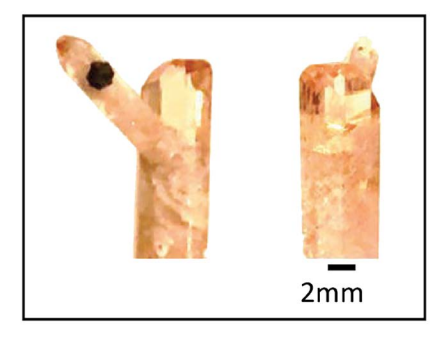


FIGURE 2. Side and front view of topaz crystal (Topaz-64) as mounted for analysis. Black cubic crystal is bixbyite. (Color online.) {{Auth: you must resupply a higher resolution figure}}

Beamline setup

The optical setup for the XFM hard X-ray microprobe from its three-polewiggler broadband source consists first of a horizontal toroidal focusing mirror to 3 gather pink beam to a secondary source aperture (SSA). The beam diverging from 4the SSA is then vertically collimated by a bent flat mirror and monochromated by a fixed-exit Si(111) double-crystal monochromator. A secondary microfocus is produced by use of an orthogonal pair of dynamically bent mirrors in KB geometry, such that beam size at the sample can be adjusted from 2 to 10 μm by adjusting 7 the SSA size at the expense of flux. Samples are mounted on a fine-resolution 8 x-y scanning stage at 45° to the incident beam, so that the sample surface can be raster-scanned with respect to the fixed beam. A 4-element Si drift detector is located in the horizontal plane at 45° to the sample (90° to the incident beam to minimize scatter) to capture fluorescence from the sample. Fluorescence signal 11 is processed by selecting element-specific fluorescence energies and normalizing 12 to incident beam intensity as measured by an ionization chamber upstream of the microfocusing mirrors.

The optical setup at the TES tender-energy microprobe beamline (Northrup 2019), co-designed as the lower-energy sister beamline to XFM at NSLS-II, consists of a bend-magnet source, vertically collimating mirror pair, fixed-exit 16 double-crystal monochromator, and vertically deflecting toroidal mirror focusing 17 to an SSA; beam diverging from the SSA is refocused by a custom set of KB mirrors to a user-tunable spot size of 2 to 10 µm. The sample chamber environment is helium at 1 atm pressure. Sample stage and detector geometry is the same as for XFM; fluorescence is measured using a Ge detector optimized for this energy range. This geometry, including the KB endstation and monochromator now at TES, was prototyped at NSLS Beamline X15B. The Al EXAFS and Si EXAFS reported here were measured at X15B; Si XANES and additional Si EXAFS were measured at TES. Si measurements used InSb monochromator crystals; Al measurements used beryl (Be3Al2Si6O18) crystals.

Data collection

XRF spectra were collected and summed over selected regions of a small ($100 \times$ 100 µm) area of Topaz-64, and of an additional topaz crystal from the same locality (Topaz-7), for comparison with concentration standards measured under identical geometric conditions. These standards are thin films of elements deposited on a polymer substrate with controlled mass per unit area, so there is no thickness effect on fluorescence, only the effects of layer ordering and of absorption by layers above 31 the element of interest. Reference films used were NIST 1833 Serial No. 991 for Fe 32 and Ti, NIST 1832 Serial No. 1294 for Mn, and MicroMatter 41156 for As and Ga.

XAS spectra for Topaz-64 were obtained by scanning incident beam energy across each element's K absorption edge while measuring fluorescence (which is directly proportional to absorption). Energy steps were larger in the pre-edge background and post-edge regions, and smaller over the absorption edge to capture 36 edge position and detailed features of XANES. For EXAFS, a longer post-edge 37 range was measured in steps calculated in constant k. EXAFS measurements of all trace elements were made in the same area of the crystal (within a radius of 150 µm) and in the same geometric orientation (Online Materials1 Table S1 provides XAS scan parameters used for each element). Fresh spots within this area 40 were used for each redox-sensitive element, to minimize the chance for radiation- 41 induced changes. Spectra were also monitored scan-to-scan for any indication of progressive changes; no evidence for beam-induced change was observed for any

The approach adopted here, microbeam XAS of a single crystal, was necessary to enable probing of microscale regions free of inclusions, but there are drawbacks to 45 this approach that must be carefully identified and mitigated. XANES and EXAFS 46 measurements of a single crystal will be sensitive to crystal orientation relative to the horizontal polarization of the incident beam (e.g., Dyar et al. 2016). All singlecrystal measurements reported here were collected with the crystal in the same orientation relative to the beam to minimize the effects of orientation-dependence. The amplitude (probability of occurrence) of each individual scattering path will 50 vary with its orientation. Scattering paths oriented vertically are least represented. This limitation is mitigated by the grouping of paths into shells, and into sets of shells sharing parameters, as discussed below. This grouping averages over a large number of paths, providing a sufficient distribution to minimize orientation effects impacting individual paths. We specifically chose the orientation of the sample, with the (110) plane at 45° to the beam and c axis vertical, because in the topaz structure that orientation gives a fairly well averaged representation of the different paths. In topaz, the crankshaft-like chains along the c axis (Fig. 1) effectively distribute most paths away from the vertical [001] vector. The symmetry of topaz indicates that sub-units alternate by 90° in orientation perpendicular to the c axis,

further averaging the orientation effects for the chosen orientation. This averaging was confirmed by the similarity between Si EXAFS of both powdered and single-crystal samples. Finally, all measurements of trace elements, and the Si reference EXAFS, were done in exactly the same orientation, validating the direct comparisons presented in this work.

For a baseline measurement of the topaz host structure, we also measured Si K-edge XANES and EXAFS of the same crystal in the same orientation, utilizing a 0.5 mm diameter beam in an area free from quartz inclusions (the larger area for these measurements is justified because any metal oxide inclusions will not contribute to the Si signal). Because the Al content limited sampling depth for Si XAS, there was no issue with self-absorption effects as might otherwise occur in an "infinitely thick" sample. For the octahedral site, we measured Al K-edge EXAFS of a powdered sample of F-topaz from a topaz rhyolite near Tepetates, San Luis Potosi, Mexico. Measurement of Al EXAFS is challenging, and further complicated by the Al-bearing beryl monochromator crystals which precluded measurement near the Al K-edge. Therefore, we were only able to measure EXAFS, not XANES, and there is inherently more uncertainty in the Al fitting results.

DATA PROCESSING

Trace element concentrations

Quantitative trace element concentrations were obtained by comparison of XRF maps of the sample and thin-film standards. For each element, fluorescence intensity of the standard was corrected for attenuation and converted to mass per unit area. This value was ratioed with fluorescence intensity in the sample and converted to mass per unit volume using a computed sampling depth (e.g., Citrin et al. 1998) with absorption data from the CXRO tool (https://henke.lbl.gov/optical_constants/atten2.html). In the absence of a reference material for Ge, the concentration was computed indirectly using a standardless method in which As concentration served as the effective standard. Germanium fluorescence intensity was ratioed to arsenic, with corrections for sampling depth, fluorescence efficiency, and absorption by the air path and detector window. The fluorescence energies of As and Ge are similar, so the corrections in the Ge calculation were relatively small.

μ-XAS spectra

The Demeter software suite (Ravel and Newville 2005) was used to process the XAS spectra. Processing started with data assessment and compilation with the Athena module. Data obtained from four detector channels were recorded; however, scans from one channel were removed from the As, Ga, and Ge data sets due to prominent diffraction artifacts spanning the data set. Individual scans were also screened for any glitches affecting more than a few energy data points, resulting in further exclusion of a handful of scans per element. After these exclusions, the usable number of scans for each element was as follows: As, 102; Fe, 61; Mn, 7; Ge, 10; Ga, 3; Ti, 38. The set of scans for each element was then merged and any remaining minor glitches edited out. Finally, pre- and post-edge (line and spline function) backgrounds were subtracted, edge steps were normalized to 1, and the Fourier transform Rbkg parameter set to 0.85 or 0.8 for each element based on the expected bond lengths for the substitution sites.

Our approach to the analysis of the μ -XAS spectra takes advantage of knowledge of the topaz structure, which provides a starting model for the two candidate cation sites. Therefore, despite the limitations of microbeam data quality and the complexities arising from orientation dependence, we are still able to address the questions of site assignment and local distortion.

XANES. Initial analysis of the merged XAS spectra focused on the XANES region. The energy position of the absorption edge of a spectrum is characteristic for a particular valence state of an element. Therefore, comparison of measured spectra with those of materials with known valence is a straightforward diagnostic tool to determine the charge of the measured element. The valence, in turn, informs preliminary assignment of the cation's structural environment, in this

case tetrahedral (the Si site) or octahedral (Al site) coordination. For elements with multiple possible oxidation states (Fe, Mn, As), the XANES region of each element's merged spectrum was compared with XANES spectra of reference standards measured under appropriate similar conditions at XFM to determine their oxidation state in topaz.

EXAFS. The merged spectra were input into the Artemis software module to determine the effect of trace element substitutions on interatomic distances. For each trace element, baseline scattering paths were calculated from trace element-free fluor-topaz crystal structure parameters of Northrup et al. (1994) by the Artemis FEFF utility, with the trace element atom substituted for Si or Al as the absorbing atom in the distorted tetrahedral or octahedral site, respectively. These paths are equivalent to the interatomic distances between the element of interest and a nearby neighbor (i.e., bond length in the case of nearest-neighbors).

For fitting, single-scattering paths from the trace element of interest were grouped into shells of similar path length (for example, the oxygen anions of the tetrahedral site comprised one shell). The geometry of the crystal was "frozen" except for linear expansion of these paths. Fitting parameters for deviation in path length compared to the baseline crystallographic model (ΔR), amplitude reduction (S0²), and sigma squared disorder parameters (σ^2) were assigned on a per-shell basis. Separate amplitude reduction variables were needed for each shell to account for orientation effects arising from measurement of an oriented single crystal. It is important to note that individual scattering paths were preserved, with the shell ΔR applied uniformly to each path within a shell. In this way, we evaluated the overall distortion of the local structure to accommodate the trace element, while significantly reducing the number of variables. This simplified fitting model limits interpretation at the scale of individual bonds but is sufficient to conclusively determine the crystallographic site hosting each trace element and to evaluate overall structural accommodations.

Shells were fit sequentially, continuing outward from the absorbing atom until data quality precluded further fitting. For the octahedral site, inclusion of both oxygen and fluorine paths in the first shell generally yielded a better fit than treating them separately. Most fits included one shell beyond the results reported here, as the overlapping contributions from the outermost shell usually improved the fit of inner shells, even when the outer shell could not be well fitted due to poorly resolved data. Notes on these partial fits, as well as any special considerations for individual elements, are presented in the results section for each element.

RESULTS

Trace element abundances

Table 1 shows the calculated concentration of each trace element, and corresponding mass exposed to the X-ray beam. For Topaz-64, arsenic was most abundant at 327 ppm, equivalent to ~12.5 pg within the sample volume analyzed, allowing for well-resolved As XAS spectra. In contrast, manganese spectra were the most difficult to resolve due to a concentration of only 9 ppm, or ~0.1 pg in the sample volume.

XAS results

The merged, deglitched XAS spectra for the trace elements studied in Topaz-64 are shown in Figure 3 (black spectra, XANES region) and Online Materials¹ Figure S2 (full spectra). These spectra were used for XANES and EXAFS analysis.

Trace element valence states determined by XANES. The topaz trace element XANES spectra were compared to reference sample spectra (Fig. 3) measured at XFM for known oxida-

TABLE 1. Measured trace element abundance for samples Topaz-64 and Topaz-7

		Conce		tion (ppm)	Element mass in vol	ume analyzed (pg)
Trace element	Computed sampling depth (µm)	Mass of topaz analyzed (ng)	Topaz-64	Topaz-7	Topaz-64	Topaz-7
As	132	38	327(16)	12.5(6)	20(1)	0.78(4)
Fe	42	12	288(9)	3.5(1)	158(5)	1.92(6)
Ga	102	29	9.4(5)	0.28(1)	6.5(3)	0.19(1)
Ge	117	34	14.8(7)	0.50(3)	14.5(7)	0.49(2)
Mn	34	10	10(1)	0.10(1)	4.4(5)	0.04(1)
Ti	16	5	79(11)	0.38(5)	125(18)	0.59(9)
Note: Mass value	s are calculated assuming a rectangula	ar beam cross section.				

20

23 24 25

26

43

44 45

46

47

48

49 50

51

52

53

54

55

56 57

58

59

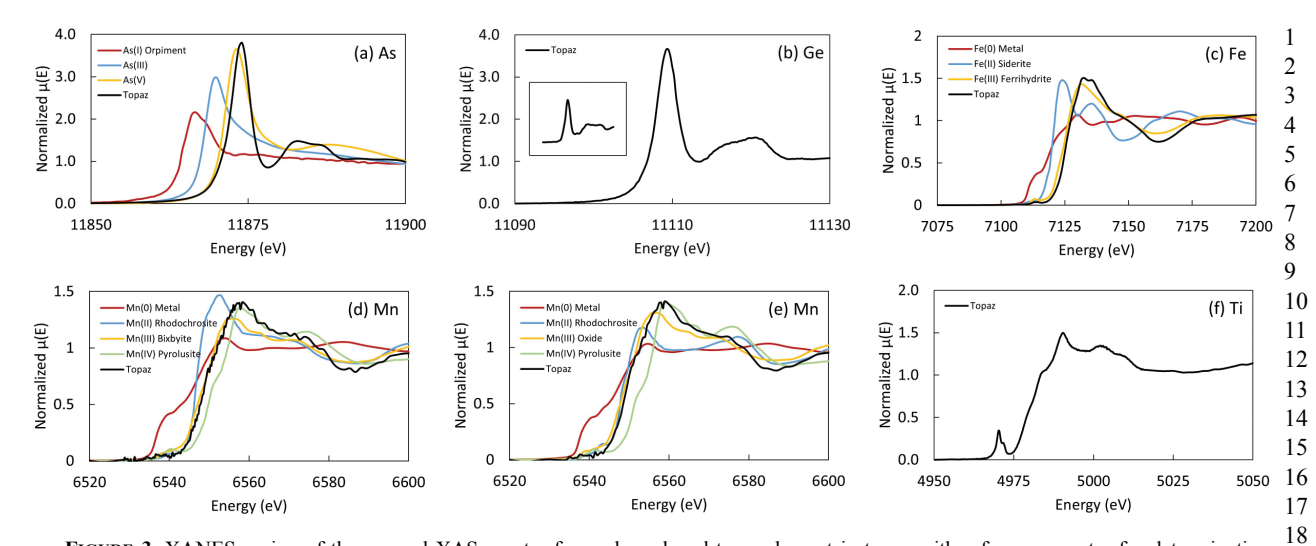


FIGURE 3. XANES region of the merged XAS spectra for each analyzed trace element in topaz with reference spectra for determination of oxidation state. (a) Arsenic data with As¹⁻ in orpiment measured in fluorescence; As³⁺ and As⁵⁺ as sodium salts dissolved in water and dried onto cellulose paper measured in transmission. (b) Germanium data; inset shows Si XANES in topaz for comparison. (c) Iron data with Fe⁰ foil measured in transmission; Fe²⁺ in siderite measured in fluorescence using a defocused beam; Fe³⁺ in ferrihydrite precipitated on quartz measured 21 in fluorescence. (d) Manganese data with Mn^0 foil measured in transmission; Mn^{2+} sulfate measured in fluorescence; Mn^{3+} in Mn_2O_3 measured in 22 fluorescence; and Mn⁴⁺ pyrolusite measured in fluorescence. (e) Titanium data. (f) Gallium data. (Color online.)

tion states. The As merged spectrum absorption edge position shows a clear match to As5+. Comparison of Fe spectra suggests Fe incorporation into topaz as ferric iron. The absorption edge position of the Mn merged spectrum offers the best agreement with Mn³⁺, consistent with the coexisting bixbyite [(Mn,Fe)₂O₃]. No valence standards were available for Ga, Ge, or Ti. Gallium and germanium are expected to be present as Ga³⁺ and Ge⁴⁺. The titanium was identifiable as Ti4+ due to the presence of a diagnostic double-peaked pre-edge feature (e.g., Farges et al. 1997).

XANES also offers a preliminary assignment of crystallographic sites for these substituents. Although oxidation state is a first-order indicator of crystallographic site, the overall shape and minor features of the XANES spectra can also be indicators as they reflect differences in coordination, symmetry and crystal field. For example, as can be seen in Figure 3, the overall spectral shapes of As (Fig. 3a) and Ge (Fig. 3b) are very similar to that of Si (Fig. 3b inset). These differ from the other XANES spectra, which are more generally similar to each other. On that basis, As and Ge likely occupy the tetrahedral site, while Fe, Mn, Ti, and Ga may occupy the octahedral site. The pre-edge peak height of the titanium is consistent with octahedral coordination (Farges et al. 1997).

Impact of trace element incorporation on local bonding 27 and geometry. EXAFS was used to definitively identify site assignments, and to assess the effect of incorporation of the trace elements studied on local bonding and geometry in the topaz structure. The first step in EXAFS analysis is conversion 31 of energy data (Online Materials¹ Fig. S2) to frequency (k), and 32 Fourier transformation to R for each element (Figs. 4, 5, and 33 6). The position of the first-shell peak and overall combination 34 of peaks in R (radial distance uncorrected for phase shift) yield characteristic visual fingerprints for tetrahedral and octahedral ³⁶ substitution sites in topaz. This allows provisional differentia- 37 tion between the tetrahedral and octahedral sites for each trace 38 element even before fitting efforts. Based on the peaks in R, the tetrahedral site contains As5+ and Ge4+ and the octahedral site Mn³⁺, Fe³⁺, Ga³⁺, and Ti⁴⁺. These assignments were confirmed by attempting to fit the data to each site model and ruling out 42 the unresolvable fit for each element.

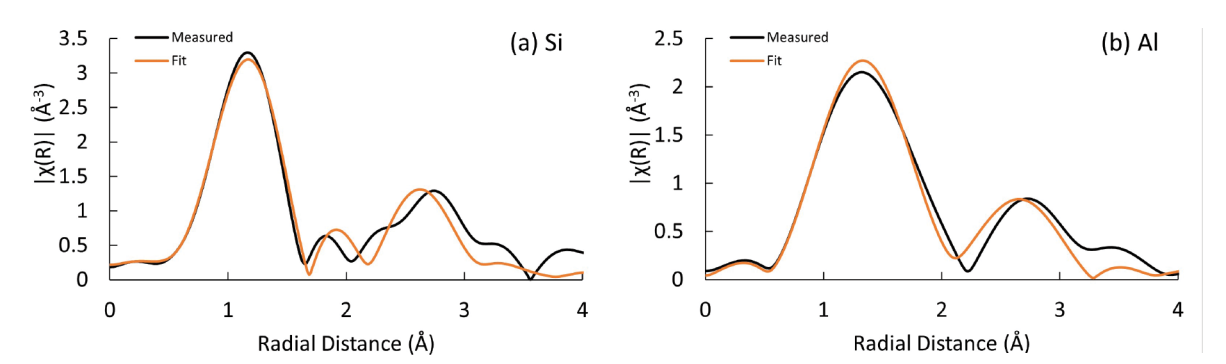


FIGURE 4. Fourier transform of Si and Al EXAFS data compared to calculated fits. This is effectively the distribution of radial distance (R) of scatterers around the absorbing atom, except distances are not corrected for phase shift. (Color online.)

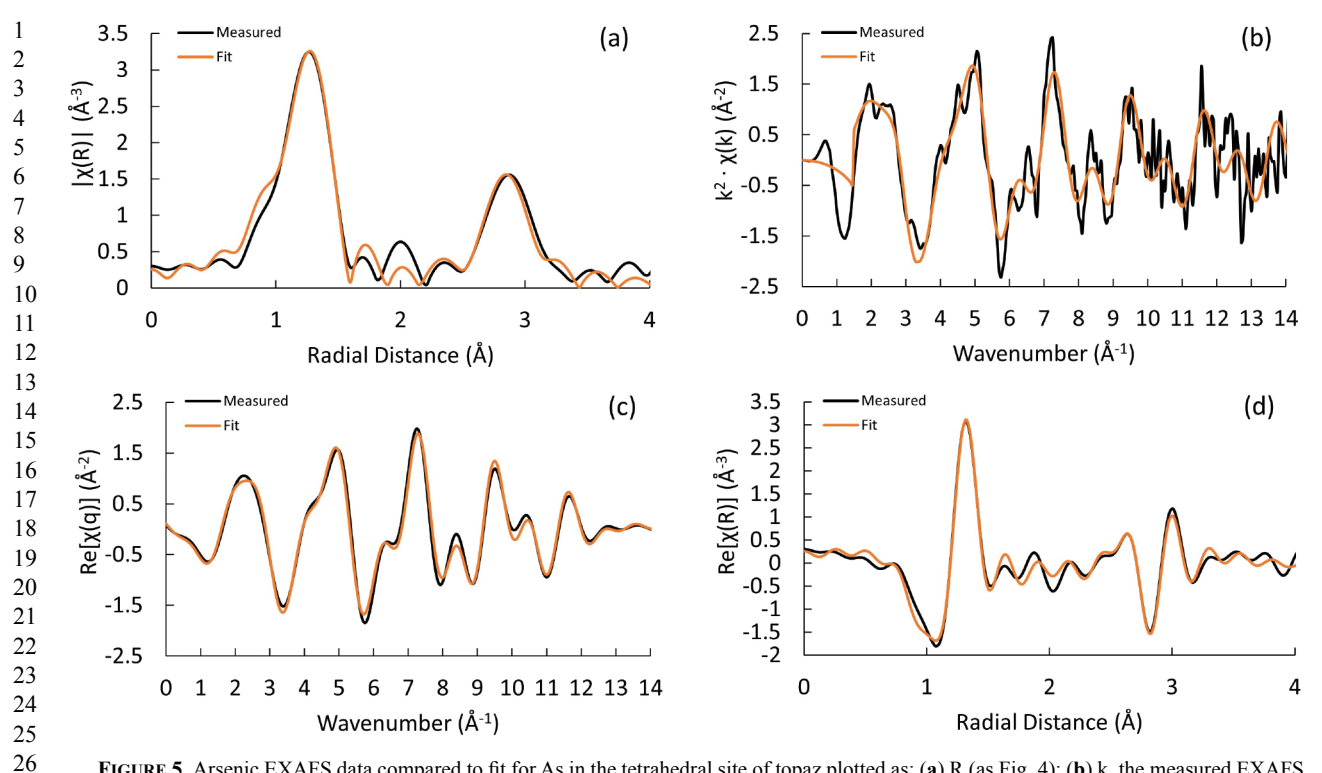


FIGURE 5. Arsenic EXAFS data compared to fit for As in the tetrahedral site of topaz plotted as: (a) R (as Fig. 4); (b) k, the measured EXAFS frequencies before Fourier transform; (c) q, the back-transform of measured data calculated from the same range of R used for fitting, i.e., Fourier filtered for direct comparison to model fit; (d) the real component of R, an indicator of fit quality. (Color online.)

Extraction of interatomic distances from EXAFS data starts with the closest coordinated anions (first shell) and proceeds to nearest neighbor cations (second shell) and a set of anions associated with those cations (third shell) as data quality permits. For this data set, acceptable fits could only be obtained out to the first or second shell, due primarily to the extremely low concentrations of most elements analyzed. To improve the quality of reported fits, and because we have independent knowledge of the host structure, fitting was generally carried out to one shell beyond the presented results. While these outer shells could not be fully resolved, they make small but significant contributions to the overall fit. In some cases, fits generated invalid negative sigma squared values. As long as the values could be positive within the uncertainty, however, we accepted these as a side effect of the somewhat disparate path

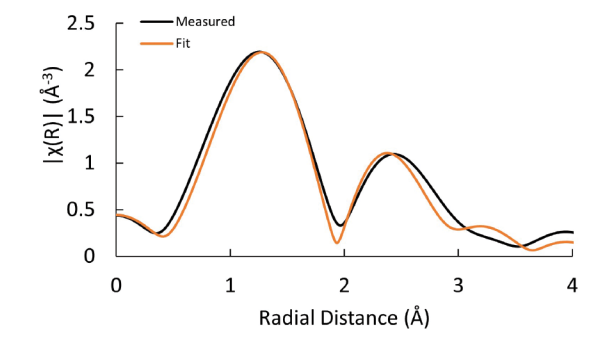


FIGURE 6. Germanium EXAFS data and fit in R (as Fig. 4) for Ge in the tetrahedral site. (Color online.)

TABLE 2. Cation-to-cation single-scattering path lengths out to second neighbors for Si and Al in fluor-topaz

	neight	ors for S	i and A	ıl ın t	luor-topaz						
Si(IV) Model			Si(IV) from EXAFS fit								
Path	R (Å)	Shell	Path	n	ΔR (Å)	σ^2 (Å ²)	SO ²				
Si-O	1.638(1)	1	Si-O	4	-0.006(13)	-0.0003(23)	-0.97(9)				
Si-O	1.642(1)										
Si-O	1.642(1)										
Si-O	1.647(1)										
Si-Al	3.174(2)	2	Si-Al	8	-0.009(26)	-0.0001(29)	-0.63(16)				
Si-Al	3.174(2)										
Si-Al	3.189(2)										
Si-Al	3.189(2)										
Si-Al	3.202(2)										
Si-Al	3.202(2)										
Si-Al	3.213(2)										
Si-Al	3.213(2)										
Al(III) Model			Al(III) from EXAFS fit								
5 11 5 18 1						2 (8 2)					

Al(III) Model			Al(III) from EXAFS fit									
Path	R (Å)	Shell	Path	n	ΔR (Å)	σ^2 (Å ²)	S0 ²					
Al-F	1.791(1)	1	Al-F	2	-0.003(11)	-0.002(2)	-0.73(8)					
Al-F	1.800(1)	1	Al-O	4	u	"	"					
Al-O	1.888(1)											
Al-O	1.895(1)											
Al-O	1.898(1)											
Al-O	1.899(1)											
Al-Al	2.810(2)	2	Al-Al	2	-0.03(4)	-0.002(6)	-0.43(25)					
Al-Al	2.839(2)	2	Al-Si	4	"	"	"					
Al-Si	3.174(2)	2	Al-Al	2	"	"	"					
Al-Si	3.189(2)											
Al-Si	3.202(2)											
Al-Si	3.213(2)											
Al-Al	3.427(2)											
Al-Al	3.427(2)											

Notes: Models are recalculated from crystallographic data (Northrup et al. 1994). Si and Al fits are from EXAFS data (this study), with model paths of similar length grouped together. Fit parameters: change in path length ΔR , disorder parameter σ^2 , and amplitude reduction S0²; degeneracy n is fixed. R-factor of Si fit is 0.087; Al, 0.025.

23

24

lengths included within some shells compounded by orientation dependence effects.

Determining the effects of trace element substitution on the topaz structure requires comparing the calculated interatomic distances from the trace element of interest to its neighbors with those of the unsubstituted cation (Al or Si) and its neighbors. To assist in these comparisons, Si and Al EXAFS data were collected for the sample and fitted in the same manner as the trace elements. Figure 4 shows the fits for Si and Al.

Table 2 shows the path lengths (R) from prior crystallographic data (single-crystal X-ray diffraction; Northrup et al. 1994) and those computed from the Si and Al EXAFS fits. The Al results are of particular note, as Al in the beryl monochromator crystals used for this energy range makes this measurement extremely difficult to obtain. We believe this to be the first reported Al Kedge EXAFS data for topaz. Variations in path length between the crystallographic model and this EXAFS fit were minimal and within the uncertainty of the fitting parameters for both Si and Al. The somewhat higher values of σ^2 (the disorder parameter) for the Al fit is to be expected given the wider spread of path lengths grouped into each shell and high correlation with the SO² (amplitude reduction) parameter. Low-SO² values for the second shells are also not unexpected and are presumed to result primarily from orientation dependence resulting from taking measurements on a single crystal.

Accommodation of trace elements in tetrahedral coordination. Figure 5 shows the EXAFS data and fit for arsenic. Fitting of the merged As spectrum was carried out to the third shell, although only the first and second were fully resolvable. Interatomic distances between As and its first and second shell neighbors increased by ~0.06 Å compared with the unsubstituted model structure (Table 3).

The germanium data set proved challenging due to its low concentration in the topaz and fewer usable scans. Figure 6 shows the R of the Ge data and the fit of the first shell. A second shell was incorporated into the fit calculations so that the shoulder underlying the first shell peak could be accounted for. The fit generated a first shell ΔR of 0.092 Å (Table 3).

Accommodation of trace elements in octahedral coordination. In the octahedral site, as had been observed for the Al fitting. the fits for the elements resulted in somewhat lower S0² values. This lends support to the suggestion that these values are predominantly a result of orientation effects rather than an issue with data quality or specific to an element. Second shell fits were more difficult in general; this is due to the larger spread of path lengths contained within the second shell and their substantial overlap and possible destructive interference with the paths of the third shell.

TABLE 3. Tetrahedral EXAFS fits, with model Si path lengths generated by Artemis FEFF calculation included for comparison

Figure 7 shows the data and fits in R for octahedral Fe, Ga,

Si(IV) Model								
Path	n	R (Å)	Shell	Path	n	ΔR (Å)	σ^2 (Å ²)	S0 ²
						As(V)		
Si-O	4	1.638-1.647	1	As-O	4	-0.060(9)	-0.0010(19)	-0.83(14)
Si-Al	8	3.174-3.213	2	As-Al	8	-0.060(19)	-0.0001(24)	-0.78(34)
						Ge(IV)		
			1	Ge-O	4	-0.092(8)	-0.001(2)	-0.96(7)

Notes: Fit parameters: change in path length ΔR , disorder parameter σ^2 , and amplitude reduction S0²; degeneracy n is fixed. R-factor of As fit is 0.021; Ge, 0.030. Mn, and Ti. Iron was fitted to the nearest-neighbor silicon sites 1 (second shell) with an unresolvable third shell. Table 4 shows the 2 computed interatomic distances. The fit produced a first shell ΔR 3 of 0.086 Å and a second shell ΔR of 0.021 Å. The Mn fit resulted 4 in a first shell ΔR of 0.034 Å. The second shell of Mn proved dif- 5 ficult. Gallium was fit out to the third shell, though here we limited 6 the number of variables by sharing fitting variables between the 7 second and third shells. Only the resulting first shell is reported, 8 with a ΔR of 0.022 Å.

The Ti fit proved uniquely challenging; a first shell fit of ac- 10 ceptable quality could not be obtained until the shorter Ti-F paths 11 and longer Ti-O paths were allowed to vary independently of each 12 other in ΔR . This resulted in a Ti-F ΔR of -0.042 Å and a Ti-O ΔR 13 of -0.113 Å, nearly doubling the difference in distance between 14 these sites compared to the aluminum and indicating a substantial 15 non-uniform distortion of the octahedron and possibly strength- 16 ening of one or both bonds to the F site (the ΔR is less than the 17 increase in ionic radius from Al³⁺ to Ti⁴⁺). This is consistent with 18 the substitution of O for F in one or both of these sites to satisfy the 19 increased bonding requirement and charge balance for Ti⁴⁺. Fitting 20 beyond the first shell was not possible, likely due to compounded 21 effects of this increased distortion of the octahedral site.

Topaz formation and gas chemistry

Topaz formation. Formation of topaz in cavities in topaz 25 rhyolite most likely involved a gas phase. The presence of gas 26 is consistent with the cavities found in the rhyolites and the 27 observation that crystals grew away from the rock interface 28 and toward the cavity and spiral-growth hillocks formed on 29 surfaces not in contact with the rhyolite. The most reasonable 30 source for this gas is local, that is, the rhyolitic magma itself. 31 Topaz formation can be envisioned as resulting from either: (1) 32 direct deposition from the cooling gas or (2) localized reaction 33 of exsolved gas with the solidified or almost solidified rhyolite. 34 Method 1 requires a significant transported load to produce 35 large crystals in small cavities. Considering gas density and the 36 low solubility of the gaseous species needed for topaz growth 37 (specifically Si and Al), a large flow-through volume would be 38 needed to provide the mass of the observed crystals. Method 2 39 can be accomplished by exsolved gas with high-HF content and 40 low transported load through a continuous cycle of local dissolu- 41 tion and precipitation that can temporarily mobilize species with 42 low solubility in the gas and redistribute them while retaining 43 HF in the gas. This is supported by observation of concentric 44 etching of the host rhyolite surrounding the original cavity as 45 evidenced by residual layers of drusy quartz crystals lining the 46 cavity, with subsequent growth of the topaz crystal into both 47 the cavity and the etched regions. The following reactions may 48 define topaz formation:

```
50
4HF (gas) + SiO_2 (rhyolite) \rightarrow SiF_4 (gas) + 2H_2O (gas)
                                                                         51
6HF (gas) + Al_2O_3 (rhyolite) \rightarrow Al_2F_6 (gas) + 3H_2O (gas)
                                                                         52
SiF_4 (gas) + 4H_2O (gas) \leftrightarrow Si(OH)_4 (gas) + 4HF (gas)
                                                                         53
      (gas-phase equilibrium)
Si(OH)_4(gas) + Al_2F_6(gas) \rightarrow Al_2SiO_4(F_2)(topaz) + 4HF(gas).
                                                                         55
```

Once a topaz crystal has nucleated, however, self-catalyzed 57 surface reactions that recycle HF would likely dominate. In 58

59

49

54

56

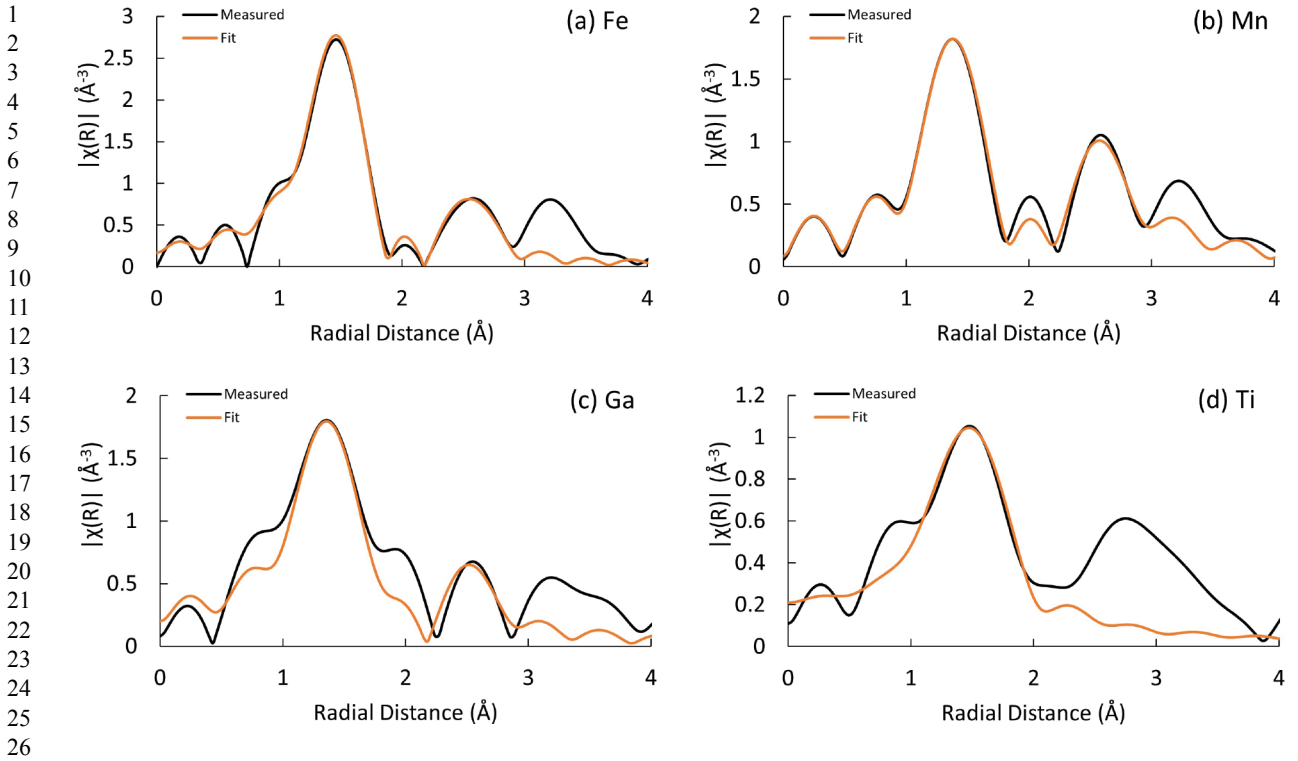


FIGURE 7. EXAFS data and fit in R (as Fig. 4) for trace elements in the topaz octahedral site (a) Fe, (b) Mn, (c) Ga, (d) Ti. (Color online.)

TABLE 4. EXAFS fits for octahedral ions, with model AI path lengths generated by Artemis FEFF calculation included for comparison

		3011						
Al(III) Model								
Path	n	R (Å)	Shell	Path	n	ΔR (Å)	σ^2 (Å ²)	SO ²
							Fe(III)	
Al-F	2	1.791-1.800	1	Fe-F	2	-0.086(6)	-0.00014(49	0.75(2)
Al-O	4	1.888-1.899	1	Fe-O	4	u	u u	"
Al-Al	2	2.810-2.839	2	Fe-Al	2	-0.021(11)	-0.0003(30)	0.53(6)
Al-Si	4	3.174-3.213	2	Fe-Si	4	"	"	"
Al-Al	2	3.427	2	Fe-Al	2	u	u	u
							Ga(III)	
			1	Ga-F	2	-0.022(11)	-0.007(2)	-0.80(8)
			1	Ga-O	4	u	u u	"
							Mn(III)	
			1	Mn-F	2	-0.034(20)	-0.001(4)	-0.52(17)
			1	Mn-O	4	u	u	"
							Ti(IV)	
			1a	Ti-F	2	-0.042(24)	-0.0022(69)	-0.60(20)
			1b	Ti-O	4	-0.113(24)	-0.0022(69)	-0.60(20)

Notes: Fit parameters: change in path length ΔR , disorder parameter σ^2 , and amplitude reduction S0²; degeneracy n is fixed. R-factor of Fe fit is 0.005; Ga 0.090; Mn 0.009; Ti 0.006.

these, -AIF on the growing surface of the topaz could react with $\mathrm{Si}(\mathrm{OH})_4$ (gas) to form an Al-O-Si bond and release HF. Subsequently, -SiOH on the surface could react with Al_2F_6 (gas) and produce a Si-O-Al bond and release HF. This process could lead to rapid growth of the observed large crystals of topaz in relatively small cavities.

The sum of the reactions given above would result in a net loss of 2HF (gas) and a net production of 1H₂O (gas) per formula unit of topaz. This would eventually deplete the HF in the gas. However, it is known that F partitions strongly into the melt in magmatic systems. Release of F from the rhyolite may be limited

by the availability of water if HF is the primary F-bearing gaseous species. Since the topaz-forming reactions produce H₂O, we can add the following reaction to maintain HF content in the gas, as this H₂O reacts with the remaining F in the rhyolite:

$$H_2O$$
 (gas) + $2F^-$ (rhyolite) $\rightarrow 2HF$ (gas) + O^{2-} (rhyolite).

This reaction could occur as the rhyolite is etched in the above process when temperatures are still 500–700 °C and would buffer the gas HF/H_2O ratio, allowing the topaz-forming reaction to continue under steady-state gas composition as long as feedstock remains available and reaction conditions (e.g., temperature) are maintained. One final consideration is that there is a parallel reaction that produces quartz:

$$Si(OH)_4$$
 (gas) $\rightarrow SiO_2$ (solid) + $2H_2O$ (gas).

This reaction provides an independent mechanism to buffer the Si content in the gas as topaz crystallizes and the rhyolite feedstock is consumed.

Insights into the gas. The topaz analyzed in this study indicates that the gas involved in its production was able to mobilize As⁵⁺, Fe³⁺, Mn³⁺, Ti⁴⁺, Ga³⁺, and Ge⁴⁺ in addition to Al and Si. XANES and EXAFS analysis showed that each of these trace elements were incorporated into the fluor-topaz structure, with the tetrahedral site containing As⁵⁺ and Ge⁴⁺ and the octahedral site Mn³⁺, Fe³⁺, Ga³⁺, and Ti⁴⁺.

Although trivalent arsenic is the dominant oxidation state in basaltic glass at 1200 °C, with pentavalent As contributing less than 10% of the budget of As (Maciag and Brenan 2020),

15

16 17

26

at lower T and high f_{O_2} , the pentavalent state is more abundant (Verweij 1980) with As5+ species such as AsO₄- in the melt. If these are also prevalent in rhyolite, then in the presence of H₂O (gas) at the surface of the rhyolite, these species may become hydrated to form AsO(OH)3. Studies of speciation and structure of As in natural melts and glasses suggest that such oxy-hydroxide complexes form strong bonds within the rhyolite glass and solids. High-HF contents may be necessary to release these to the gas (e.g., Pokrovski et al. 2002; Testemale et al. 2004; {{AU: Reference not in list. Please add.}} Borisova et al. 2010; James-Smith et al. 2010). Local transport of released AsO(OH)₃ and precipitation of As in topaz by an HF-rich gas can be envisioned by the reaction:

$$AsO(OH)_3 (gas) + Al_2F_6 (gas) + H_2O (gas) \rightarrow Al_2AsO_4(FO)$$

(topaz) + 5HF (gas).

although it is more likely that -Al-F species on the surface of the growing topaz react with AsO(OH)3. This reaction reflects the coupled substitution needed for As5+ to substitute for Si4+ in the tetrahedral site, most likely the substitution of an O²⁻ for F⁻ (or OH-) at one of the two "F apices" of a neighboring octahedron (Fig. 1) for charge balance. In spite of the required coupled substitution, the As content $(327 \pm 16 \text{ ppm})$ is the highest of all of the trace elements analyzed here in Topaz-64 (Table 1). Arsenic contents in topaz can be quite variable, however. Table 1 also shows the trace element content of Topaz-7; its arsenic concentration is only 20 ± 1 ppm. This difference in As content could be explained by topaz with lower As growing earlier since a higher As content in the gas would result from continued precipitation of non-As bearing phases.

Like As5+, Ge4+ substitutes for Si, although its slightly greater ionic radius induces a slightly greater expansion of the structure upon substitution (as indicated by the slightly longer Ge-O bond relative to the As-O bond in Table 3). The similarity in size of As⁵⁺ and Ge⁴⁺ and their joint preference for the tetrahedral site, however, suggest that their solubilities in topaz should be similar. Therefore, the much lower Ge^{4+} content (14.8 \pm 0.7 ppm, Topaz-64; 14.5 ± 0.7 ppm, Topaz 7) compared with As⁵⁺ content $(327 \pm 16 \text{ ppm}, \text{Topaz-64})$ suggests several possibilities: (1) that the gas may not have inherited much Ge from the rhyolite source; (2) the Ge⁴⁺ content of the gas was being buffered by the presence of a condensed phase, leading to a concentration far below saturation; or (3) for some unknown reason, the tetrahedral site in topaz cannot accommodate much Ge⁴⁺. Breiter et al. (2013b) documented Ge⁴⁺ contents as high as 204 ppm in topaz that is, much closer to what we observed for As5+. This excludes possibility 3 and is consistent with a similar partitioning potential of As⁵⁺ and Ge4+ into topaz. Although only two topaz crystals were analyzed here—too few to draw a robust conclusion—possibility 2 seems most likely, as the same concentration of Ge4+ in both crystals suggests that the Ge concentration in the two topaz crystals analyzed was buffered through the precipitation of another Ge-bearing mineral phase in which $a_{Ge}^{S} < <1$, such as quartz, magnetite (e.g., Meng et al. 2017), hematite (e.g., Bernstein and Waychunas 1987), cassiterite, or bixbyite (see summary of Höll et al. 2007). All of these phases have been found associated with topaz rhyolite (Burt et al. 1982; Christiansen et al. 1984). In fact,

as noted above, a crystal of bixbyite was attached to one of the 1 topaz samples analyzed here (Fig. 2), and quartz was associated 2 with both samples. Such buffering of Ge⁴⁺ activity would inhibit 3 the relative Ge⁴⁺ content of the gas from increasing much during 4 precipitation of nominally Ge-free phases.

Of the trace elements preferentially partitioning into the octa- 6 hedral site, Fe³⁺ has the greatest abundance in the topaz crystals 7 analyzed. The structural effects of Fe³⁺ substitution diminish fur- 8 ther away from the cation (Table 4). These observations suggest 9 primarily an effect of a larger ionic radius with little distortion 10 of the structure. Formation of the Fe³⁺ topaz component is likely 11 facilitated through the reaction of HF with the rhyolite, perhaps 12 through the following reactions:

```
6HF (gas) + Fe<sub>2</sub>O<sub>3</sub> (rhyolite) \rightarrow Fe<sub>2</sub>F<sub>6</sub> (gas) + 3H<sub>2</sub>O (gas)
Si(OH)_4 (gas) + Fe_2F_6 (gas) \rightarrow Fe_2SiO_4(F_2) (topaz) + 4HF (gas).
```

This topaz component may also be formed by -Si-O on the 18 topaz surface reacting locally with Fe₂F₆ in the gas. Although the 19 Fe concentrations in the topaz crystals analyzed are high (Fe³⁺: 288 ± 9 ppm, Topaz-64; 158 ± 5 ppm, Topaz-7), they do not 21 approach the more than 400 ppm of Fe³⁺ that has been observed 22 in other topaz crystals (Breiter et al. 2013b). This suggests that 23 when this topaz formed, hematite was not yet precipitating and 24 that the ferric iron content of the gas continued to increase during 25 formation of Fe-poor precipitates.

The minor perturbation of the topaz structure by Ga³⁺ and 27 Mn³⁺ substitution for Al³⁺ (Table 4) suggests that topaz should 28 be able to accommodate a significant amount of both. The much 29 lower concentration of Ga³⁺ than Fe³⁺ for both crystals analyzed 30 suggests a lower Ga³⁺ concentration in the rhyolite source, 31 consistent with generally low Ga contents of felsic rocks (e.g., 32 Breiter et al. 2013b) and possibly coupled with lower partitioning 33 of Ga³⁺ into the gas. The much lower Mn³⁺ abundance relative to 34 Fe³⁺ is more difficult to explain since the presence of coexisting 35 bixbyite in Topaz-64 suggests a high load of Mn locally in the gas 36 and that Topaz-64 was saturated in Mn. The low concentration 37 of Mn in topaz at saturation with bixbyite may be caused by the 38 symmetry-lowering Jahn-Teller distortion of Mn³⁺ in octahedral 39 coordination (e.g., Halcrow 2013; Fridrichová et al. 2018). This 40 Jahn-Teller distortion is likely incompatible with the octahedral 41 distortion inherent to the topaz structure caused by two shorter 42 F apices and may thus reduce the compatibility of Mn with the 43 topaz structure, leading to low solubility. In comparison, beryl, 44 formed under similar conditions in topaz rhyolite but with a less 45 distorted AlO₆ octahedral site, can incorporate much higher Mn 46 contents (e.g., Sardi and Heimann 2014; over 300 ppm Mn³⁺ in 47 beryl from Utah topaz rhyolite measured for this work). The 48 low solubility of Mn in topaz observed here is consistent with 49 the typical low Mn contents for topaz from anorogenic granite 50 (Breiter et al. 2013b).

Ti⁴⁺ substitution for Al in the octahedral site in topaz must 52 be a coupled substitution in which one of the apical F⁻ (or OH⁻) 53 ions of the octahedron is replaced by O²⁻ for charge balance. As 54 shown in Table 4, the cation-F bond in the octahedron is shorter 55 than the cation-O bond. In a fully relaxed structure, the substitution 56 of O²⁻ for F⁻ (or OH⁻) would thus lengthen the bond, but the topaz 57 structure does not permit this, and the Ti-O bond in an F site will 58

51

6

7

8

Q

10

11

12

13

14

15

16

17

18

19

20

21

22

23

24

25

26

27

28

29

30

31

32

33

34

35

36

37

38

39

40

41

42

43

44

45

46

47

48

49

50

51

52

53

54

55

56

remain shortened. This is effectively a Ti=O double bond, common in Ti-bearing phases (e.g., titanite, Speer and Gibbs 1976). which satisfies the increased bonding needs for Ti⁴⁺ in that site.

In late-stage rhyolite melt, Ti⁴⁺ may be in fivefold-coordinated complexes with four bridging and one non-bridging O bonds (e.g., Ackerson et al. 2020) that are tightly bound and likely show little solubility in the exsolving gas. This may account for the observation that Ti abundance is low in the gas phase (e.g., Symonds and Reed 1993; Shevko et al. 2018). In spite of these complexities, Ti⁴⁺ contents are quite variable in topaz and can reach 480 ppm (Gauzzi and Graça 2018), suggesting that the Ti contents in the topaz studied here had not reached saturation in Ti⁴⁺ content.

Perhaps in spite of low-Ti solubility in gas, locally, the reaction of an HF-rich gas with Ti-bearing rhyolitic glass, ilmenite (or hematite with an ilmenite component) could release Ti⁴⁺ to form a gaseous species such as TiF₄. This may produce the Ti topaz component through a reaction such as:

 $Si(OH)_4 (gas) + 2TiF_4 (gas) + 2H_2O (gas) = Ti_2SiO_4(OO)$ (topaz) + 8HF (gas).

IMPLICATIONS

This work has demonstrated that synchrotron-based microbeam XAS studies on picogram abundances of trace elements in single crystals can yield definitive information on their oxidation states, site occupancy, and the local structural perturbations that they induce. It documents the substitution of arsenic for silicon in a common silicate mineral. This work also presents the first synchrotron-based Al EXAFS analysis of topaz. In addition to improving our understanding of structural accommodation of trace elements in minerals, this work shows the potential of using trace elements in minerals to constrain the compositional characteristics of dilute gases involved in their formation and to gain insights into the gas-mediated processes that lead to mineral precipitation and alteration in the shallow subvolcanic environment. This study opens up new directions in the exploration of these processes.

ACKNOWLEDGMENTS

The authors thank G. Lamble and J.-F. Lee for their help and expertise in the initial EXAFS measurements of bulk topaz (Northrup et al. 1995), which established the foundation for our current work. We appreciate Tiffany Victor's assistance in measuring some of the oxidation state standards.

FUNDING

Support for this work was provided through grants EAR 1725212 (to H.N.) and EAR 2105876 (to H.N. and P.N.) via the Petrology and Geochemistry Program of the National Science Foundation. This research used the XFM and TES beamlines of the National Synchrotron Light Source II, and Beamline X15B of the National Synchrotron Light Source, U.S. Department of Energy (DOE) Office of Science User Facilities operated for the DOE by Brookhaven National Laboratory under Contract Nos. DE-SC0012704 and DE-AC02-98CH10886, respectively. Measurements supported by the Tender Energy Microspectroscopy Consortium.

REFERENCES CITED

- Ackerson, M.R., Cody, G.D., and Mysen, B.O. (2020) 29Si solid state NMR and Ti K-edge XAFS pre-edge spectroscopy reveal complex behavior of Ti in silicate melts. Progress in Earth and Planetary Science, 7, 14-25, https://doi.org/ 10.1186/s40645-020-00326-2
- Agangi, A., Kamenetsky, V.S., Hofmann, A., Przybylowicz, W., and Vladykin, N.V. (2014) Crystallization of magmatic topaz and implications for Nb-Ta-W mineralization in F-rich silicic melts—the Ary-Bulak ongonite massif. Lithos, 202-203, 317-330, https://doi.org/10.1016/j.lithos.2014.05.032.
- Alston, N.A. and West, J. (1928) The structure of topaz. Proceedings of the Royal Society of London, 121, 358-367.

- Bernstein, L. and Waychunas, G. (1987) Germanium crystal chemistry in hematite and goethite from the Apex mine Utah, and some new data on germanium in aqueous solution and in stottite. Geochimica et Cosmochimica Acta, 51, 623-630, https://doi.org/10.1016/0016-7037(87)90074-3.
- Bikun, J.V. (1980) Fluorine and lithophile element mineralization at Spor Mountain, Utah. U.S. Department of Energy Open-File Report GJBX-225(80), 167–377.
- Borisova, A.Y., Pokrovski, G.S., Pichavant, M., Freydier, R., and Candaudap, F. (2010) Arsenic enrichment in hydrous peraluminous melts: Insights from femtosecond laser ablation inductively coupled plasma-quadrupole mass spectrometry, and in situ X-ray absorption fine structure spectroscopy. American Mineralogist, 95, 1095-1104, https://doi.org/10.2138/am.2010.3424.
- Bove, D.J., Mast, M.A., Dalton, J.B., Wright, W.G., and Yager, D.B. (2007) Major styles of mineralization and hydrothermal alteration and related solid- and aqueous-phase geochemical signatures. In S.E. Church, P. von Guerard, and S.E. Finger, Eds., Integrated Investigations of Environmental Effects of Historical Mining in the Animas River Watershed, San Juan County, Colorado. U.S. Geological Survey Professional Paper 1651, 165-230.
- Breiter, K., Gardenová, N., Kanický, V., and Vaculovič, T. (2013a) Gallium and germanium geochemistry during magmatic fractionation and post-magmatic alteration in different types of granitoids: A case study from the Bohemian Massif (Czech Republic). Geologica Carpathica, 64, 171-180, https://doi.org/ 10.2478/geoca-2013-0018.
- Breiter, K., Gardenová, N., Vaculovič, T., and Kanický, V. (2013b) Topaz as an important host for Ge in granites and greisens. Mineralogical Magazine, 77. 403-417, https://doi.org/10.1180/minmag.2013.077.4.01.
- Burt, D.M. and Sheridan, M.F. (1981) A model for the formation of uranium/ lithophile element deposits in fluorine-enriched volcanic rocks. American Association of Petroleum Geologists Studies in Geology, 13, 99-109.
- Burt, D.M., Sheridan, M.F., Bikun, J.V., and Christiansen, E.H. (1982) Topaz rhyolites; distribution, origin, and significance for exploration. Economic Geology and the Bulletin of the Society of Economic Geologists, 77, 1818-1836, https:// doi.org/10.2113/gsecongeo.77.8.1818.
- Christiansen, E.H., Bikun, J.V., and Burt, D.M. (1980) Petrology and geochemistry of topaz rhyolites, western United States. U.S. Department of Energy Open-File Report GJBX, 225, 37-122.
- Christiansen, E.H., Bikun, J.V., Sheridan, M.F., and Burt, D.M. (1984) Geochemical evolution of topaz rhyolites from the Thomas Range and Spor Mountain, Utah. American Mineralogist, 69, 223-236.
- Citrin, P.H., Northrup, P., Atkins, R.M., Glodis, P.F., Niu, L., Marcus, M.A., and Jacobson, D.C. (1998) Characterizing trace metal impurities in optical waveguide materials using X-ray absorption. Proceedings of the Materials Research Society, 524, 251-257, https://doi.org/10.1557/PROC-524-251.
- Dyar, M.D., Breves, E., Gunter, M., Lanzirotti, A., Tucker, J., Carey, C., Peel, S., Brown, E., Oberti, R., Lerotic, M., and others. (2016) Use of multivariate analysis for synchrotron micro-XANES analysis of iron valence state in amphiboles. American Mineralogist, 101, 1171-1189, https://doi.org/10.2138/ am-2016-5556
- Farges, F., Brown, G.E. Jr., and Rehr, J.J. (1997) Ti K-edge XANES studies of Ti coordination and disorder in oxide compounds: Comparison between theory and experiment. Physical Review B: Condensed Matter, 56, 1809-1819, https:// doi.org/10.1103/PhysRevB.56.1809.
- Fridrichová, J., Bacik, P., Ertl, A., Wildner, M., Dekan, J., and Miglierini, M. (2018) Jahn-Teller distortion of Mn3+-occupied octahedra in red beryl from Utah indicated by optical spectroscopy. Journal of Molecular Structure, 1152, 79-86, https://doi.org/10.1016/j.molstruc.2017.09.081
- Gauzzi, T. and Graça, L. (2018) A cathodoluminscence-assisted LA-ICP-MS study of topaz from different geological settings. Brazilian Journal of Geology, 48, 161–176, https://doi.org/10.1590/2317-4889201820170127.
- Goad, B.E. and Černy, P. (1981) Peraluminous pegmatitic granites and their pegmatite aureoles in the Winnipeg River district, southeastern Manitoba. Canadian Mineralogist, 19, 177–194
- Groat, L.A., Turner, D.J., and Evans, R.J. (2014) Gem deposits. Treatise on Geochemistry, 13, 595-622, https://doi.org/10.1016/B978-0-08-095975-7.01126-8.
- Halcrow, M.A. (2013) Jahn-Teller distortions in transition metal compounds, and their importance in functional molecular and inorganic materials. Chemical Society Reviews, 42, 1784-1795, https://doi.org/10.1039/C2CS35253B.
- Holfert, J. (1978) A field guide to topaz and associated minerals of Topaz Mountain, Utah. John Holfert. {{AU: Add publisher name? Or is it self-published?}}
- Höll, R., Kling, M., and Schroll, E. (2007) Metallogenesis of germanium—A review. Ore Geology Reviews, 30, 145-180, https://doi.org/10.1016/j. oregeorev.2005.07.034
- James-Smith, J., Cauzid, J., Testemale, D., Liu, W., Hazemann, J.-L., Proux, O., Etschmann, B., Philippot, P., Banks, D., Williams, P., and others. (2010) Arsenic speciation in fluid inclusions using microbeam X-ray absorption spectroscopy. American Mineralogist, 95, 921–932, https://doi.org/10.2138/am.2010.3411.
- Kovalenko, V.L. and Kovalenko, N.I. (1976) Ongonites—subvolcanic analogues of rare metal lithium-fluorine granites. Joint Soviet-Mongolian Scientific Research Geol. Expedition. Trans-Action 15.
- Lindsey, D.A. (1977) Epithermal beryllium deposits in waterlaid tuff, western Utah.

15

18

20

21

22

23

24

26

28

29

30

31

32

33

34

35

36

37

38

39

- Economic Geology and the Bulletin of the Society of Economic Geologists, 72, 219-232, https://doi.org/10.2113/gsecongeo.72.2.219
- (1982) Tertiary volcanic rocks and uranium in the Thomas Range and northern Drum Mountains, Juab County, Utah. U.S. Geological Survey Professional Paper, 1221, https://doi.org/10.3133/pp1221.
- Lipman, P.W., Christiansen, R.L., and Van Alstine, R.E. (1969) Retention of alkalis by calc-alkalic rhyolites during crystallization and hydration. American Mineralogist, 54, 286-291.
- Maciag, B.J. and Brenan, J.M. (2020) Speciation of arsenic and antimony in basaltic magmas. Geochimica et Cosmochimica Acta, 276, 198-218, https:// doi.org/10.1016/j.gca.2020.02.022.
- Meng, Y., Hu, R., Huang, X., and Gao, J. (2017) Germanium in magnetite: A preliminary review. Acta Geologica Sinica, 91, 711-726, https://doi.org/ 10.1111/1755-6724.13127.
- Newville, M. (2008) Fundamentals of XAFS. Consortium for Advanced Radiation Sources, University of Chicago, https://docs.xrayabsorption.org/tutorials/ XAFS Fundamentals.pdf.
- Northrup, P. (2019) The TES beamline (8-BM) at NSLS-II: Tender-energy spatially resolved X-ray absorption spectroscopy and X-ray fluorescence imaging Journal of Synchrotron Radiation, 26, 2064-2074, https://doi.org/10.1107/ S1600577519012761.
- Northrup, P.A. and Reeder, R.J. (1994) Evidence for the importance of growthsurface structure to trace element incorporation in topaz. American Mineralogist, 79, 1167-1175.
- (1995) Relationship between the structure and growth morphology of topaz [Al₂SiO₄(OH,F)₂] using the periodic bond chain method. Journal of Crystal Growth, 156, 433-442, https://doi.org/10.1016/0022-0248(95)00287-1.
- Northrup, P.A., Leinenweber, K., and Parise, J.B. (1994) The location of H in the high-pressure synthetic Al₂SiO₄(OH)₂ topaz analogue. American Mineralogist, 79, 401-404.
- Northrup, P.A., Lamble, G., Lee, J.-F., and Reeder, R.J. (1995) An XAFS study of arsenic substitution for silicon in topaz [Al₂SiO₄(F,OH)₂]. 1995 Goldschmidt Conference Program and Abstracts, 76.
- O'Bannon, E.F. III and Williams, Q. (2019) A Cr3+ luminescence study of natural topaz Al₂SiO₄(F,OH)₂ up to 60 GPa. American Mineralogist, 104, 1656–1662, https://doi.org/10.2138/am-2019-7079.
- Pauling, L. (1928) The crystal structure of topaz. Proceedings of the National Academy of Sciences, 14, 603-606, https://doi.org/10.1073/pnas.14.8.603
- Penfield, S.L. and Minor, J.C. (1894) On the chemical composition and related physical properties of topaz. American Journal of Science, s3-47, 387-396.
- Pokrovski, G.S., Zakirov, I.V., Roux, J., Testemale, D., Hazemann, J.L., Bychkov, A.Y., and Golikova, G.V. (2002) Experimental study of arsenic speciation in vapor phase to 500 °C: Implications for As transport and fractionation in lowdensity crustal fluids and volcanic gases. Geochimica et Cosmochimica Acta, 66, 3453-3480, https://doi.org/10.1016/S0016-7037(02)00946-8.
- Ravel, B. and Newville, M. (2005) ATHENA, ARTEMIS, HEPHAESTUS: Data analysis for X-ray absorption spectroscopy using IFEFFIT. Journal of Synchrotron Radiation, 12, 537-541, https://doi.org/10.1107/S0909049505012719.
- Ribbe, P.H. and Gibbs, G.V. (1971) The crystal structure of topaz and its relation to physical properties. American Mineralogist, 56, 24-30.
- Roedder, E. and Stalder, H.A. (1988) "Pneumatolysis" and fluid-retention evidence for crystal growth from a vapor phase. In M. Santosh, Ed., Fluid Inclusions, M-11, 1-12. Geological Society of India.
- Rossman, G.R. (2011) The color of topaz. In J. Clifford, A.U. Falster, S. Hanson,

- S. Liebtrau, G. Neumeier, and G. Staebler, Eds., Topaz: Perfect Cleavage, 1 79-85. Lithographie.
- Sardi, F. and Heimann, A. (2014) Pegmatitic beryl as indicator of melt evolution: Example from the Velasco District, Pampeana pegmatite province, Argentina, and review of worldwide occurrences. Canadian Mineralogist, 52, 809, https:// doi.org/10.3749/canmin.1400032.
- Schott, S., Rager, H., Schürmann, K., and Taran, M. (2003) Spectroscopic 5 study of natural gem quality "Imperial" topazes from Ouro Preto, Brazil. 6 European Journal of Mineralogy, 15, 701-706, https://doi.org/10.1127/0935-1221/2003/0015-0701
- Shevko, E.P., Bortnikova, S.B., Abrosimova, N.A., Kamenetsky, V.S., Bortnikova, S.P., Panin, G.L., and Zelenski, M. (2018) Trace elements and minerals in fumarolic sulfur: The case of Ebeko Volcano, Kuriles. Geofluids, 2018, 4586363, https://doi.org/10.1155/2018/4586363.
- Speer, J.A. and Gibbs, G.V. (1976) The crystal structure of synthetic titanite, 11 CaTiOSiO₄, and the domain textures of natural titanites. American Mineralogist, 61, 238-247.
- Staatz, M.H. and Carr, W.J. (1964) Geology and mineral deposits of the Thomas and Dugway Ranges, Juab and Tooele Counties, Utah. U.S. Geological Survey 14 Professional Paper 415, https://doi.org/10.3133/pp415.
- Symonds, R.B. and Reed, M.H. (1993) Calculation of multicomponent chemical equilibria in gas-solid-liquid systems: Calculation methods, thermochemical 16 data and applications to studies of high-temperature volcanic gases with examples from Mount St. Helens. American Journal of Science, 293, 758-864, https://doi.org/10.2475/ajs.293.8.758.
- Testemale, D., Pokrovski, G.S., and Hazemann, J.L. (2011) Speciation of AsIII 19 and AsV in hydrothermal fluids by in situ X-ray absorption spectroscopy. European Journal of Mineralogy, 23, 379–390, https://doi.org/10.1127/0935-1221/2011/0023-2104. {{AU: Call out not found in paper. Please add or delete.}}
- Thomas, R. (1982) Ergebnisse der thermobarogeochemischen Untersuchungen an Flüssigkeitseinschlüssen in Mineralen der postmagmatischen Zinn-Wolfram Mineralisation des Erzgebirges. Freiberger Forschungshefte, 370.
- Verweij, H. (1980) Melting and fining of arsenic-containing silicate glass batches. Ph.D. thesis, Technische Hogeschool Eindhoven. https://doi.org/10.6100/ IR95983
- 27 Wasim, M., Zafar, W., Tufail, M., Arif, M., Daud, M., and Ahmad, A. (2011) Elemental analysis of topaz from northern areas of Pakistan and assessment of induced radioactivity level after neutron irradiation for color induction. Journal of Radioanalytical and Nuclear Chemistry, 287, 821-826, https://doi.org/ 10.1007/s10967-010-0879-8.
- Wyckoff, R.W.G. (1969) Crystal Structures, 4, 174. {{AU: Please provide publisher and number of pages.}}

MANUSCRIPT RECEIVED DECEMBER 15, 2021 MANUSCRIPT ACCEPTED DECEMBER 23, 2021 ACCEPTED MANUSCRIPT ONLINE JANUARY 12, 2023 MANUSCRIPT HANDLED BY DANIEL R. NEUVILLE

Endnote:

¹Deposit item AM-23-128417. Online Materials are free to all readers. Go online via the table of contents or article view, and find the tab or link for supplemental